RAA 2014 Vol. **14** No. **10**, 1234–1250 doi: 10.1088/1674–4527/14/10/003
http://www.raa-journal.org *http://www.iop.org/journals/raa*

Research in Astronomy and Astrophysics

A search for double-peaked narrow emission line galaxies and AGNs in the LAMOST DR1 *

Zhi-Xin Shi[1,2,3], A-Li Luo[1], Georges Comte[1,4], Xiao-Yan Chen[1], Peng Wei[1,3], Yong-Heng Zhao[1], Fu-Chao Wu[2], Yan-Xia Zhang[1], Shi-Yin Shen[5], Ming Yang[1], Hong Wu[1], Xue-Bing Wu[6], Hao-Tong Zhang[1], Ya-Juan Lei[1], Jian-Nan Zhang[1], Ting-Gui Wang[7], Ge Jin[7] and Yong Zhang[8]

[1] Key Laboratory of Optical Astronomy, National Astronomical Observatories, Chinese Academy of Sciences, Beijing 100012, China; *lal@lamost.org*
[2] National Laboratory of Pattern Recognition, Institute of Automation, Chinese Academy of Sciences, Beijing 100190, China
[3] University of Chinese Academy of Sciences, Beijing 100049, China
[4] Aix-Marseille Université & CNRS, Institut Pythéas, LAM (Laboratoire d'Astrophysique de Marseille), UMR7326, F-13388 Marseille, France
[5] Shanghai Astronomical Observatory, Chinese Academy of Sciences, Shanghai 200030, China
[6] Department of Astronomy, Peking University, Beijing 100871, China
[7] University of Science and Technology of China, Hefei 230026, China
[8] Nanjing Institute of Astronomical Optics & Technology, National Astronomical Observatories, Chinese Academy of Sciences, Nanjing 210042, China

Received 2014 January 2; accepted 2014 April 21

Abstract The Large Sky Area Multi-Object Fiber Spectroscopic Telescope (LAMOST) has released more than two million spectra, which provide the opportunity to search for double-peaked narrow emission line (NEL) galaxies and active galactic nuclei (AGNs). The double-peaked narrow-line profiles can be well modeled by two velocity components, respectively blueshifted and redshifted with respect to the systemic recession velocity. This paper presents 20 double-peaked NEL galaxies and AGNs found from LAMOST DR1 using a search method based on a multi-Gaussian fit of the narrow emission lines. Among them, ten have already been published by other authors, either listed as genuine double-peaked NEL objects or as asymmetric NEL objects, and the remaining ten are original discoveries. We discuss some possible origins for the double-peaked narrow-line features, such as interaction between jet and narrow line regions, interaction with companion galaxies, and black hole binaries. Spatially resolved optical imaging and/or follow-up observations in other spectral bands are needed to further discuss the physical mechanisms at work.

Key words: galaxies: emission lines — quasars: emission lines — methods: data analysis

* Supported by the National Natural Science Foundation of China.

1 INTRODUCTION

The search for double-peaked narrow-line structures in galaxy spectra is an effective way for finding candidates of binary active galactic nuclei (AGNs) (Zhou et al. 2004; Blecha et al. 2013), which are expected to be formed in the final phases of the merging of two interacting active galaxies. Since the suggestion that double-peaked profiles could be produced by binary AGNs (Zhou et al. 2004), much attention has been paid to this hypothesis, yet few definite cases are known. The most convincing examples can be found in CXO J1426+35 (Barrows et al. 2012), EGSD2 J1420+4259 (Gerke et al. 2007), NGC 6240 (Komossa et al. 2003), COSMOS J100043+020637 (Comerford et al. 2009b), SDSS J0952+2552 (McGurk et al. 2011; Fu et al. 2012) and so on (see the review in Wang & Zhou 2012, and table 1 in Ge et al. 2012). Several systematic searches for AGNs with double-peaked [O III] emission lines have been performed in the DEEP2 survey sample (Gerke et al. 2007; Comerford et al. 2009a) and in the Sloan Digital Sky Survey (hereafter SDSS) data releases (Xu & Komossa 2009; Wang et al. 2009; Liu et al. 2010b,2011; Smith et al. 2010; Ge et al. 2012). The last authors retrieved a large sample of 3030 dual-peak narrow emission line (NEL) objects from the SDSS DR7, and a much larger sample of asymmetric profiles in NEL objects, with in total 54 dual-core candidates. Among the candidates found at low or moderate redshift, when a double-peaked [O III] emission line had been suspected or was confirmed as an indicator of a binary AGN, the components most likely traced objects with spatial separations in the range from 100 pc to 10 kpc (Wang et al. 2009).

However, a double-peaked NEL can also be produced by other mechanisms, such as chance superposition, peculiar gas kinematics in the narrow-line regions (NLRs; e.g., Gelderman & Whittle 1994; Fu & Stockton 2009; Fischer et al. 2011; Shen et al. 2011; Fu et al. 2012) or jet-cloud interactions (e.g., Stockton et al. 2007; Rosario et al. 2010). Because of the growing interest in double-peaked NEL objects, it is also important to check that the candidates are fully trustworthy, thus independent surveys should confirm this. In order to further analyze these double-peaked samples, follow-up observations are needed. Previous works have used various methods, such as high-resolution optical imaging (Comerford et al. 2009b), near-infrared imaging (Liu et al. 2010b; Fu et al. 2011a; Rosario et al. 2011; Shen et al. 2011; Barrows et al. 2012), integral-field spectroscopy (Fu et al. 2012), hard X-ray observations (Comerford et al. 2011; Civano et al. 2012; Liu et al. 2013), radio observations (Zhou et al. 2004; Fu et al. 2011b), and long slit spectroscopy (Shen et al. 2011; Comerford et al. 2012).

In this paper, we focus on a systematic search for galaxies and AGNs with double-peaked NELs in the First Data Release of the Sky Survey conducted with the Large Sky Area Multi-Object Fiber Spectroscopic Telescope (LAMOST, also called the Guo Shou Jing Telescope, GSJT), hereafter LAMOST DR1. Like the SDSS, LAMOST has produced a large number of quasar and galaxy spectra from October 2011 to June 2013 (its first two observing seasons). We have developed a method to search for double-peaked NEL galaxies and AGNs in LAMOST DR1, and visually inspected the candidate spectra for confirmation. Our sample selection and method are described in Section 2. We present and discuss the results in Section 3, and compare them to results derived from SDSS spectra where available. We summarize this work in Section 4.

2 SAMPLE SELECTION

2.1 LAMOST

LAMOST has the capability of taking 4000 spectra of objects distributed across a 20 square degree field simultaneously in a single exposure. The spectral range extends from 3700 Å to 9000 Å with a resolution of $R = 1800$. The telescope, fiber positioning system and its spectrographs are described in detail in Cui et al. (2012).

A spectroscopic survey of over 10 million objects started in autumn 2012, focusing on stellar astrophysics, the structure of the Milky Way, and extragalactic astrophysics and cosmology (Zhao et al. 2012). A limited Pilot Survey dedicated to the test of data processing pipelines and exhaustive performance evaluation was first launched on 2011 Oct 24, and ended in June 2012, including nine lunar cycles and basically covering the best observing period available in a year at the Xinglong Observing Station (Yao et al. 2012; Luo et al. 2012). In autumn 2012, LAMOST began a general survey. The first public release, DR1 (July 2013), contains more than two million spectra.

The raw data are reduced with LAMOST 2D and 1D pipelines (Luo et al. 2004, 2012), including bias subtraction, cosmic-ray removal, spectrum extraction, flat-fielding through twilight exposures, wavelength calibration, sky subtraction and multiple exposure co-addition. The LAMOST pipeline only provides a relative flux calibration, hence, for the 17 objects for which SDSS spectra are available, we have used the SDSS fluxes to rescale the relative LAMOST fluxes to the absolute flux scale of SDSS.

2.2 Method

We start from the spectral sample of LAMOST DR1, including 12 082 galaxies and 5017 quasars. In order to select double-peaked NEL candidates, we have developed a reduction method inspired by the work of Ge et al. (2012).

2.2.1 Sample trimming

We first trim the DR1 extragalactic sample with the following criteria, applied to all preselected spectra:

(1) across the rest-frame wavelength ranges [4700, 5100] Å and [6500, 6800] Å (i.e. the regions containing respectively Hβ- [O III]and Hα- [S II] emission lines) the average signal-to-noise ratio (S/N) per pixel of the continuum must be > 2;
(2) rest-frame equivalent widths (EWs) of the emission lines must obey: EW (Hα, Hβ, [O III] λ5007) $>$3 Å;
(3) to ensure that [O III] emission lines are included in the observed wavelength range, we initially cut the redshift at $z < 0.9$.

This preselection procedure provided a reduced sample of around 6000 galaxies and 3000 QSOs. After visually inspecting each spectrum of LAMOST and selecting those suspected of hosting a double NEL, we were left with about 150 galaxies and 50 QSOs, which were then submitted to the following operation.

2.2.2 Starlight subtraction

The spectra from LAMOST are taken through a $3.3''$ diameter fiber, large enough to include the light from the nucleus and stellar light from the host galaxy. Absorptions can mask or weaken the emissions, and the stellar continuum can also affect the measurement of emission-line intensities. To obtain reliable values of emission-lines fluxes, the underlying stellar continuum is first removed using a spectral synthesis model.

(a) We first correct the foreground Galactic extinction using the reddening maps of Schlegel et al. (1998).

(b) We shift the spectra back to the rest frame defined by a systemic redshift value automatically produced by the LAMOST data processing pipeline. This redshift is fully consistent with the value attached to objects in the SDSS, which has 17 objects in common.

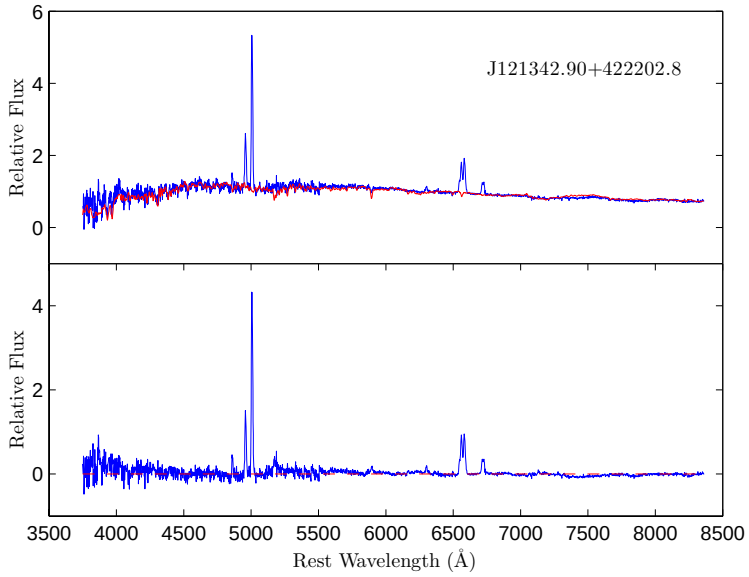

Fig. 1 Example of spectral fitting applied to the host galaxy with stellar population templates (BC03, Bruzual & Charlot 2003) using the STARLIGHT code. In the top panel, the blue line is the observed spectrum, and the red line is the model spectrum of the galaxy (*color online*). The bottom panel shows the residuals, i.e., the spectrum after starlight is subtracted.

(c) The STARLIGHT software (Cid Fernandes et al. 2005) is then used to fit the continuum and stellar absorption lines and continua from the underlying stellar population. STARLIGHT generates a model spectrum M_λ by co-adding up to N_* instantaneous starburst models (Simple Stellar Populations, SSPs) with different ages and metallicities from the evolutionary synthesis models of Bruzual & Charlot (2003). This model is fitted to the observed spectrum O_λ in which emission lines, night sky line residuals and possible bad pixels have been masked out (see details in Chen et al. 2009), using the Metropolis scheme which searches for the minimum $\chi^2 = \Sigma_\lambda[(O_\lambda - M_\lambda)\omega_\lambda]^2$, where ω_λ^{-1} is the error in O_λ, not counting masked regions. Among the various options that can be selected, we use the reddening law of CCM (Cardelli et al. 1989), the Padova 1994 tracks (Alongi et al. 1993), and the Chabrier (Chabrier 2003) initial mass function. Moreover, we use 45 SSPs, which include 15 different ages from 1 Myr to 13 Gyr and three different metallicities (0.2, 1 and 2.5 $Z_\odot$).

An example of starlight subtraction is shown in Figure 1, which exhibits both the result of a fit to the continuum and absorption lines (top panel) and the spectrum after the starlight is subtracted (bottom panel). This latter component is then submitted to the following procedure.

2.2.3 Multi-gaussian fitting

We fit each individual detected emission line with three models: a single Gaussian, a double Gaussian and a double Gaussian plus an additional broader wing that is also a Gaussian. The F-test is employed to decide which model has statistically the highest probability of being the best representation of the data. One calculates the F-value with the following equation

$$F = \frac{(\mathrm{SSE_{m1}} - \mathrm{SSE_{m2}})/(\mathrm{DoF_{m1}} - \mathrm{DoF_{model2}})}{\mathrm{SSE_{m2}}/\mathrm{Dof_{m2}}}, \quad (1)$$

where $\mathrm{SSE_{m1}}$ is the residual sum of squares for the simple Gaussian model and $\mathrm{SSE_{m2}}$ is for the complex Gaussian model. DoF is the number of degrees of freedom of each model (i.e. the number of data points used in the fit minus the number of function parameters used). A larger F-value indicates that the complex Gaussian model has a higher probability to be correct than the single Gaussian one.

After we excluded the possibility of a single Gaussian model, we use a free parameter set to fit each emission line, and adopted them as the initial values for our fixed fitting technique. The "blue" (i.e. blueshifted from the adopted reference systemic redshift) and "red" (representing redshifted) Gaussian systems show their respective consistency in that both have the same center wavelength shift and the same full width at half maximum (FWHM).

Finally, we visually inspect all the fits and verify that the line profiles are correctly fitted by the model. Then, we match the results with the corresponding spectrum from SDSS to confirm the double NEL. There are 20 double-peaked NEL objects, and Figure 2 shows five examples from the galaxy subsample.

2.2.4 Comparison with SDSS spectra

In the present sample, objects detected as having double-peaked NELs are located in the footprint of the SDSS, with 17 having a spectrum in SDSS DR9 and among these, ten were already identified with double-peaked NELs or strongly asymmetric NELs (see Table 2 for references). We have collected the 17 SDSS spectra and have independently applied the same procedure to them, which fully confirms the double-peaked nature of the narrow emission lines, ruling out possible noise or reduction artifacts. We have also checked the consistency of the results derived from LAMOST and SDSS data on the velocity differences between the NEL components and on the emission line ratios of each NEL component. We obtain

$$\Delta V_{\mathrm{LAMOST}} = (0.94 \pm 0.10) \cdot \Delta V_{\mathrm{SDSS}} + (125 \pm 30) \tag{2}$$

with ΔV in $\mathrm{km\ s^{-1}}$, and

$$\log([\mathrm{OIII}]5007/\mathrm{H}\beta)_{\mathrm{LAMOST}} = (0.91 \pm 0.05) \cdot \log([\mathrm{OIII}]5007/\mathrm{H}\beta)_{\mathrm{SDSS}} + (0.05 \pm 0.03), \tag{3}$$

$$\log([\mathrm{NII}]6584/\mathrm{H}\alpha)_{\mathrm{LAMOST}} = (0.91 \pm 0.06) \cdot \log([\mathrm{NII}]6584/\mathrm{H}\alpha)_{\mathrm{SDSS}} - (0.02 \pm 0.02). \tag{4}$$

3 RESULTS AND DISCUSSIONS

3.1 Optical Data

We find a total of 20 double-peaked NEL objects, 15 galaxies and five QSOs, which are listed in Table 1. Among these, ten have already been published by other authors, and the remaining ten are original discoveries. Three new spectra were first observed by LAMOST, see Figure 3. All our candidates have a high S/N with an average r-band magnitude (in the SDSS system) of $\overline{r}$ = 17.17.

Figure 4(a) shows their redshift distribution, which is strongly bimodal because of our selection criteria. Objects with $0.5 \leq z \leq 0.7$ are all optically unresolved QSOs, for which the emission complex Hα - [N II] is shifted beyond the available spectral range. The double-peaked NEL characteristic of these objects is only determined from the profiles of [O III]$\lambda\lambda$ 4959, 5007 and the narrow component of Hβ. An additional constraint is added to the initial trimming criteria (Sect. 2.2.1 above) because of the poor quality of the LAMOST spectra beyond 8500 Å, with a redshift cut at $z = 0.7$ so that [O III]λ5007 is measurable in good conditions. Objects with $z \leq 0.2$ are resolved galaxies on the SDSS images. To ensure a reliable identification of double NEL, we require that not only Hβ and [O III] $\lambda\lambda$ 4959, 5007, but also [N II]$\lambda\lambda$ 6548, 6584, Hα and [S II]$\lambda\lambda$ 6717, 6731 all present double-peaked narrow-line profiles, and for these we require an additional constraint that [S II]λ 6731 <8500 Å. Note that this difference in selection criteria between galaxies and QSOs is

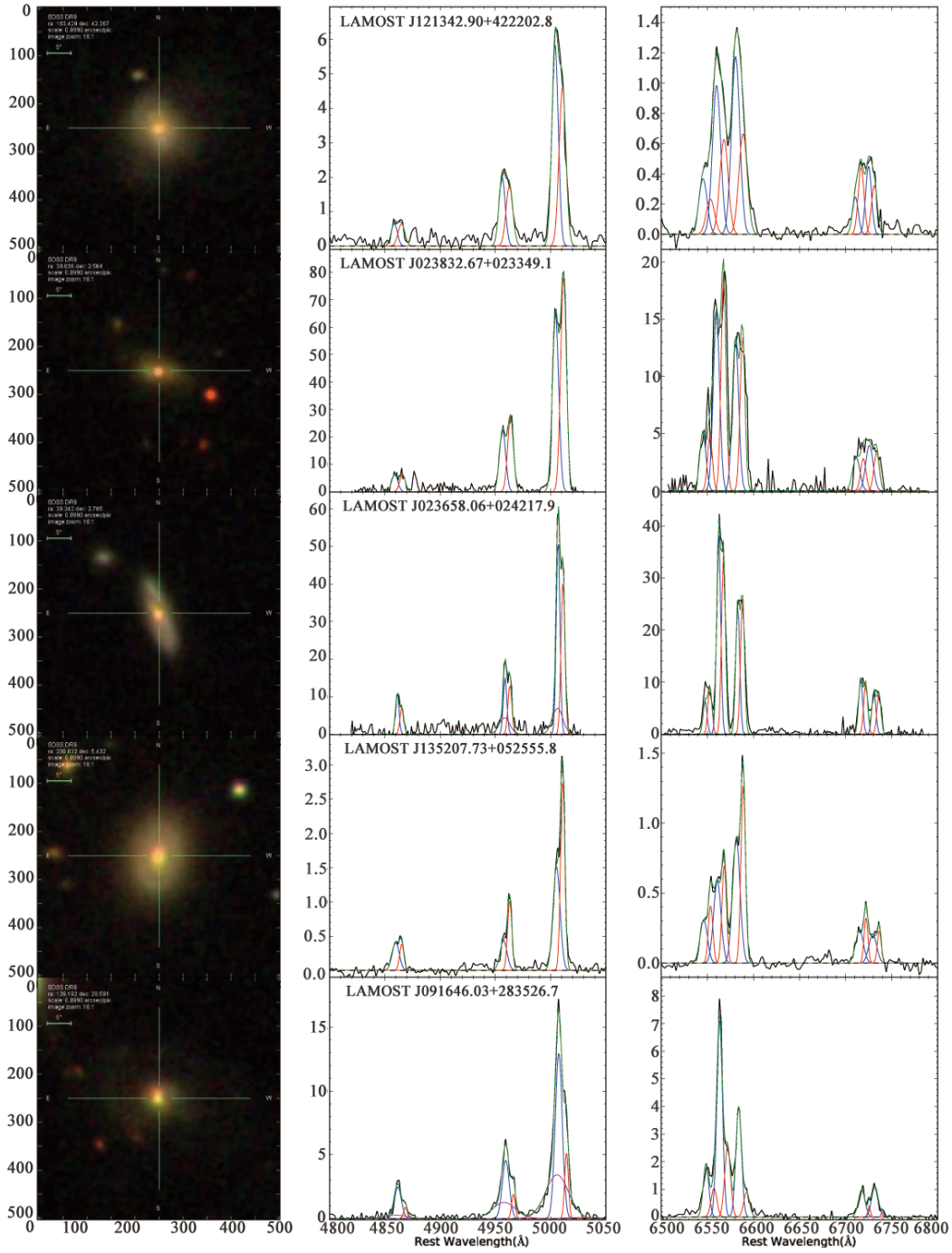

Fig. 2 SDSS images (*left*) and spectra (*right*) of five examples with double-peaked emission lines. *Black*: original spectra, *blue*: the blue component, *red*: the red component, magenta: the wing of the emission lines, *green*: sum of all the components.

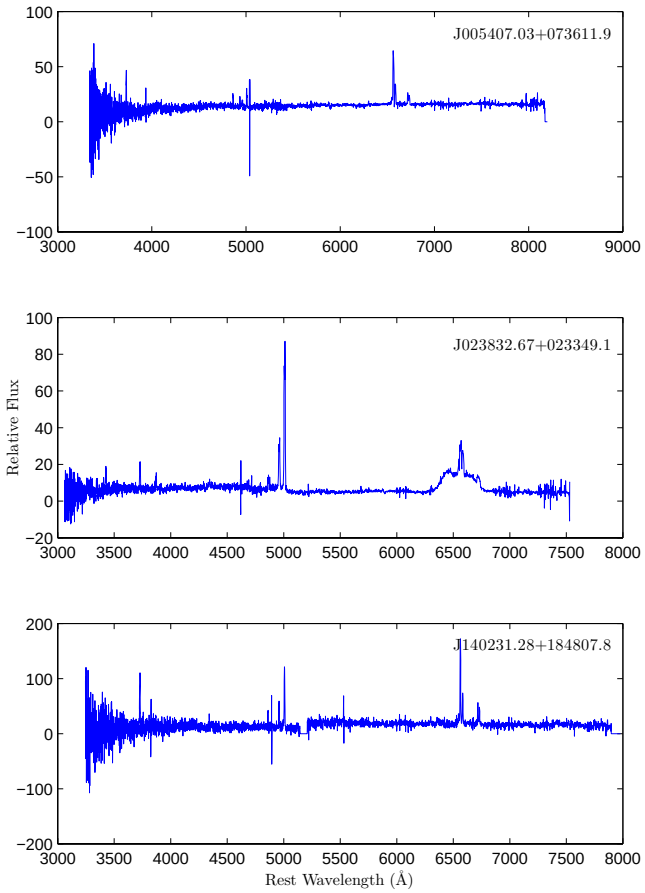

Fig. 3 Totally, 20 double-peaked NEL objects were found from LAMOST DR1. Among the first ten discoveries, three new spectra were first observed by LAMOST and are presented here.

motivated by the data quality: in LAMOST DR1, the bulk of the redshift distribution of QSOs is clearly higher than that of the galaxies (at a given average magnitude) and the S/N of QSO spectra is generally better than that of galactic nuclei, probably because of the illumination conditions of the entrance face of the fiber.

Figure 4(b) shows the distribution of the velocity differences between the two components of the NEL. The distribution is roughly symmetric around a mean value of $\langle \Delta V \rangle = 280\ \mathrm{km\ s^{-1}}$. There is no significant difference in the observed $\langle \Delta V \rangle$ between QSOs and galaxies. The spectral resolution of LAMOST corresponds to an average instrumental FWHM of 3.5 Å, i.e. 200 $\mathrm{km\ s^{-1}}$on the [O III]λ5007 at the average redshift of the galaxy subsample (for higher z or lines in the red range the instrumental constraints are less stringent). The accuracy of centering to achieve a good S/N for a Gaussian component having such an FWHM, with the usual computer algorithms, is roughly 1/10 of the FWHM, and degrades when the S/N weakens. Hence we are confident that all our detected double peaked NELs listed in Table 2 are reliable. Furthermore, the same procedures applied to the 17 objects that have a spectrum in the SDSS DR9 yielded consistent results with those listed in Table 2, confirming the double peaked character of the NEL. Finally, two objects, J121342+4222

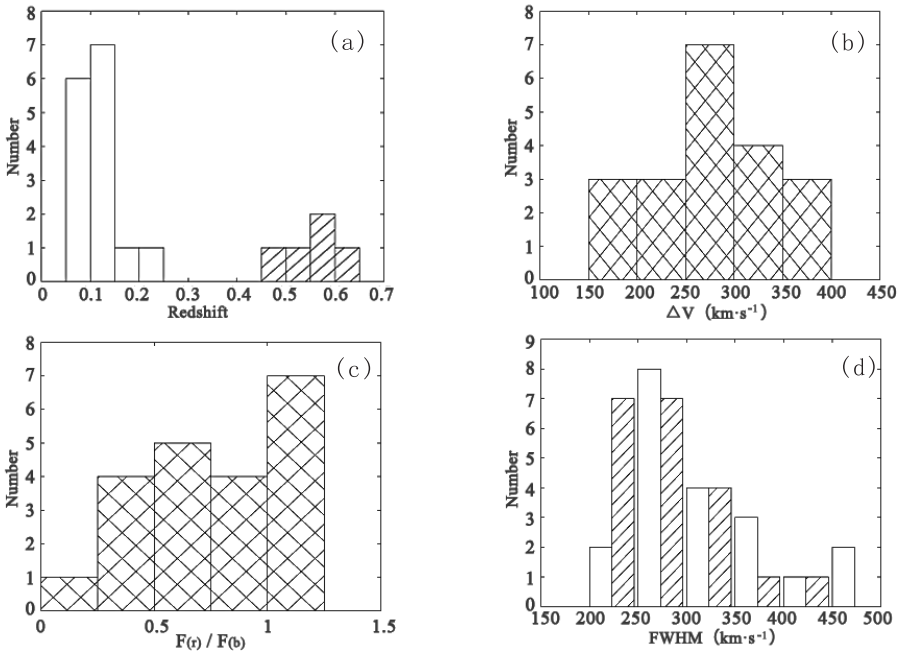

Fig. 4 The distribution of our double-peaked objects. (a) redshift distribution of galaxies (*empty bars*) and QSOs (*bars with hatched lines*); (b) distribution of velocity difference between NEL components; (c) flux ratio of the red and blue [O III] components; (d) FWHM distribution of blue (*empty bars*) and red (*bars with hatched lines*) components.

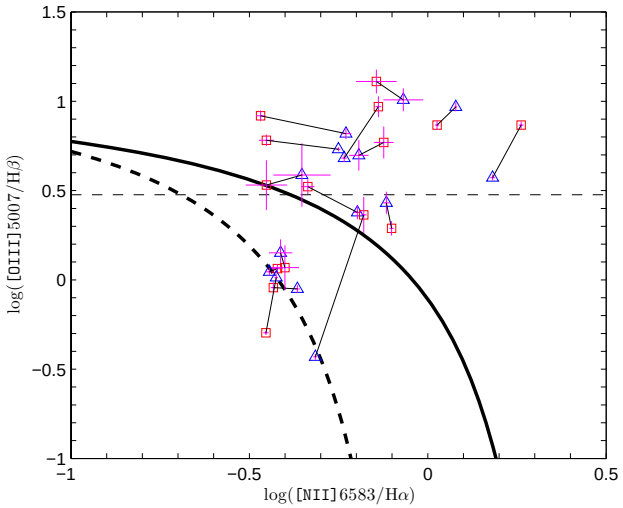

Fig. 5 The BPT diagnostic diagram for objects with measured [N II] and Hα emission lines (14 objects). For each object, a blue triangle indicates the low velocity component and the red square indicates the high velocity one. Two components belonging to the same source are connected by a thin continuous black line. The error bars are shown in magenta. The solid curve defined by Kewley et al. (2001) and the dashed curve defined by Kauffmann et al. (2003) show the separation between star-forming galaxies, composite galaxies and AGNs. The horizontal dotted line is defined by [O III] / Hβ = 3. This line is often suggested to separate Seyferts from LINERS.

Table 1 List of Double-peaked NEL Sample in LAMOST DR1

Designation (1)	Obs. Date (2)	MJD (3)	Plate (4)	SPID (5)	FIB (6)	Type (7)	z (8)	r (9)	SDSS (10)
J005407.03+073611.9	20121108	56240	EG010249N073002F	14	047	G	0.10719	17.05	0
J023658.06+024217.9	20121114 (*)	56246	EG023131N032619F	06	232	G	0.08744	16.17	1
J023832.67+023349.1	20121114	56246	EG023131N032619F	06	206	G	0.20780	17.13	0
J083425.28+283451.3	20130113	56306	HD083217N291909F01	08	157	G	0.10253	17.04	1
J091646.03+283526.7	20120201	55959	B5595902	15	006	G	0.14233	16.63	1
J094430.79+435421.4	20130215	56339	HD094642N450651F01	05	088	Q	0.58779	17.77	1
J100708.01+242039.0	20130401	56384	HD100153N235852F01	09	134	Q	0.54355	18.81	1
J104718.31+254348.3	20130210	56334	HD104049N254200F01	09	237	Q	0.62712	18.72	1
J113630.61+135848.8	20130214	56338	HD112941N152447F01	07	088	G	0.08169	16.91	1
J121342.90+422202.8	20130307 (**)	56359	HD121906N401846F01	16	245	G	0.07525	15.46	1
J123314.49+262624.9	20130111	56304	HD122624N271605F01	06	006	Q	0.57025	18.58	1
J131434.73+563419.3	20130430	56413	HD132545N565813F01	10	239	G	0.14407	17.39	1
J133730.29–002525.4	20130406	56389	HD134427N004207F01	10	050	G	0.17212	17.11	1
J133737.82+555816.7	20130430	56413	HD132545N565813F01	06	023	Q	0.47461	19.26	1
J135207.73+052555.8	20130409	56392	HD135024N052949M01	04	239	G	0.07892	15.01	1
J135646.10+102609.0	20120514	56062	VB3_210N09_V2	14	091	G	0.12313	15.81	1
J140225.68+465817.4	20130310	56362	HD141351N461930F01	14	218	G	0.12759	16.79	1
J140231.28+184807.8	20130210	56334	HD140137N164527F01	11	118	G	0.13970	18.95	0
J150501.56+371311.7	20130402	56385	HD145553N362548F01	13	109	G	0.06517	16.25	1
J232703.17+004256.7	20121024	56225	EG232111N021150M01	07	073	G	0.06601	16.47	1

Notes: Column (1) LAMOST DR1 designation hhmmss.ss+ddmmss.s (J2000.0); Col. (2) Date of observation; Cols. (3)–(6) the MJD, Plate, Spectrograph id and Fiber id in the LAMOST Sky Survey; Col. (7) Type: G: galaxy nucleus, Q: QSO; Col. (8) redshift; Col. (9) apparent magnitude in r-band (in the SDSS system); Col. (10) 1 or 0 means that the object has a spectrum in SDSS DR9 (1) or not (0). (*) also observed on 20130501, (**) also observed on 20121113.

and J023658+0242, have been observed twice by LAMOST and the data as well as the fitting results of the two-epoch spectra are consistent.

Figure 4(c) shows the distribution of the intensity ratios of the "blue" and "red" NEL velocity components in the [O III]λ5007 line. About 50% of the objects in our sample have a flux ratio between 0.75 and 1.25. Smith et al. (2012) argue that double peaked AGNs in which the two narrow line components have closely similar intensities often represent rotating disks, and are inconsistent with a black hole binary scenario. There remain 50% of objects, in which the "blue" component flux is stronger than the "red" component one. If a simple interaction between the radio jet and the NLR was at work, (see also Sect. 3.4.2 below) the "blue" component should be systematically stronger than the "red" component. Figure 4(d) shows the distributions of the FWHM of the "blue" and "red" NEL velocity components. Most objects exhibit intrinsically narrow lines, with FWHM $\leq$ 300 $\mathrm{km\ s^{-1}}$on both components.

Figure 5 shows, for the objects belonging to the *galaxy* subsample, the location of the two NEL components in the 1981 (hereafter BPT) emission line diagnostic diagram. We recall that there is still some debate about the accuracy of the distinction between AGN and starburst (or HII-like) spectra in the BPT diagram, with the theoretical dividing line as derived by Kewley et al. (2001) being largely offset from the empirical dividing line derived by Kauffmann et al. (2003) from a very large sample of emission-line galaxies. In seven objects, both components are clearly located in the Kewley et al. AGN region, implying that the ionization of their narrow-line plasma is dominated by non-thermal sources. Note that, from only this diagram, the contribution from radiative shock cannot be evaluated quantitatively. Three other objects have their two components close to the Kewley et al. separation line between the AGN-like spectra and the thermal HII-like spectra, but inside the Kauffmann et al.

Table 2 Emission Line Properties of the Double-peaked Emission Line Sample

Designation	NEL model	ΔV	FWHM$_b$	FWHM$_r$	$F^b_{[\mathrm{O\,III}]}/F^b_{\mathrm{H}_\beta}$	$F^r_{[\mathrm{O\,III}]}/F^r_{\mathrm{H}_\beta}$	$F^b_{[\mathrm{N\,II}]}/F^b_{\mathrm{H}_\alpha}$	$F^r_{[\mathrm{N\,II}]}/F^r_{\mathrm{H}_\alpha}$	Type	Ref
(1)	(2)	(3)	(4)	(5)	(6)	(7)	(8)	(9)	(10)	(11)
J005407.03+073611.9	2G	279 ± 44	301 ± 43	224 ± 48	1.42 ± 0.25	1.17 ± 0.34	0.39 ± 0.03	0.40 ± 0.04	SF + SF	–
J023658.06+024217.9	2G + W	250 ± 49	236 ± 44	241 ± 33	4.99 ± 0.99	5.88 ± 1.21	0.64 ± 0.04	0.75 ± 0.05	AGN + AGN	–
J023832.67+023349.1	2G	378 ± 83	397 ± 53	325 ± 39	10.20 ± 1.49	12.91 ± 1.99	0.85 ± 0.11	0.72 ± 0.09	AGN + AGN	–
J083425.28+283451.3	2G	294 ± 43	296 ± 16	346 ± 53	0.37 ± 0.02	2.31 ± 0.54	0.48 ± 0.01	0.66 ± 0.01	SF + Comp	[4]b
J091646.03+283526.7	2G + W	392 ± 17	391 ± 15	251 ± 29	5.39 ± 0.14	6.05 ± 0.44	0.56 ± 0.01	0.35 ± 0.02	AGN + AGN	[2]
J094430.79+435421.4	2G + W	306 ± 16	280 ± 15	255 ± 21	4.81 ± 1.03	9.24 ± 4.32	–	–	–	–
J100708.01+242039.0	2G + W	340 ± 25	373 ± 80	230 ± 115	3.87 ± 1.74	3.43 ± 0.71	–	–	–	[3]
J104718.31+254348.3	2G + W	249 ± 58	252 ± 46	270 ± 59	6.31 ± 2.27	13.38 ± 9.54	–	–	–	–
J113630.61+135848.8	2G	192 ± 39	322 ± 33	301 ± 30	2.70 ± 0.39	1.94 ± 0.18	0.77 ± 0.02	0.79 ± 0.01	Comp + Comp	[1]
J121342.90+422202.8	2G	349 ± 88	414 ± 72	425 ± 44	9.30 ± 0.54	7.36 ± 0.43	1.20 ± 0.01	1.06 ± 0.02	AGN + AGN	–
J123314.49+262624.9	2G + W	253 ± 16	297 ± 23	239 ± 17	7.56 ± 0.66	7.41 ± 0.63	–	–	–	–
J131434.73+563419.3	2G	181 ± 21	282 ± 25	251 ± 19	0.89 ± 0.05	0.91 ± 0.06	0.43 ± 0.01	0.37 ± 0.01	SF + SF	[4]b
J133730.29–002525.4	2G	239 ± 18	267 ± 19	230 ± 18	2.39 ± 0.21	3.33 ± 0.31	0.64 ± 0.02	0.46 ± 0.02	Comp + Comp	[4]b
J133737.82+555816.7	2G + W	265 ± 28	314 ± 21	327 ± 31	8.92 ± 4.83	3.05 ± 0.65	–	–	–	–
J135207.73+052555.8	2G	331 ± 16	450 ± 20	263 ± 9	3.74 ± 0.15	7.36 ± 0.36	1.52 ± 0.03	1.83 ± 0.03	AGN + AGN	[1], [4]a
J135646.10+102609.0	2G + W	386 ± 23	484 ± 23	394 ± 26	6.59 ± 0.46	8.29 ± 0.57	$0.59 \pm 0.02*$	$0.34 \pm 0.01*$	AGN + AGN	[2]
J140225.68+465817.4	2G	224 ± 42	281 ± 20	260 ± 24	1.03 ± 0.04	0.51 ± 0.02	0.38 ± 0.01	0.35 ± 0.01	SF + SF	–
J140231.28+184807.8	2G + W	156 ± 109	203 ± 74	207 ± 72	3.86 ± 1.58	3.39 ± 1.09	0.44 ± 0.08	0.35 ± 0.05	Comp + Comp	–
J150501.56+371311.7	2G	256 ± 39	287 ± 19	292 ± 37	4.81 ± 0.23	9.33 ± 1.25	0.58 ± 0.01	0.73 ± 0.02	AGN + AGN	[4]b
J232703.17+004256.7	2G	267 ± 18	332 ± 16	235 ± 16	1.11 ± 0.05	1.16 ± 0.06	0.36 ± 0.01	0.38 ± 0.01	SF + SF	[4]a

Notes: Column (1) LAMOST DR1 designation hhmmss.ss+ddmmss.s (J2000.0); Col. (2) Best NEL model: 2G: 2 Gaussians, 2G+W: 2 Gaussian + a broader Gaussian "wing"; Col. (3) velocity difference in $\mathrm{km\ s^{-1}}$between the two NEL components, in the rest frame defined by the redshift listed in Table 1; Cols. (4)–(5) FWHMs of blue and red components, in units of $\mathrm{km\ s^{-1}}$; Cols. (6)–(7) flux ratio of [O III] λ 5007 and Hβ; Cols. (8)–(9) flux ratio of [N II] λ 6583 and Hα. Notes: * indicates that the values are from the spectrum provided by SDSS for technical reasons; Col. (10) Location of NEL components in the BPT diagram: AGN: AGN-like line ratios, SF: likely dominated by massive star formation, Comp: on the Kewley et al. (2001) AGN-HII separation line, possibly composite or transitional (in Kauffmann et al. (2003) these would be classified AGNs); Col. (11) [1]: Wang et al. 2009, [2]: Liu et al. 2010a, [3]: Smith et al. 2010, [4] Ge et al. 2012: a) listed as double-peaked NEL, b) listed as asymmetric NEL.

AGN region. For these objects, a significant contribution from thermal photoionization by ongoing massive star formation is possible. One object (J083425+283451) exhibits widely different behavior in its two NEL components, with the "blue" one probably being largely dominated by thermal photoionization, and the "red" one being transitional, or AGN-like, on the Kewley et al. separation line. The four remaining objects have their NEL components clustered in a small area of the diagram, with a small dispersion around [O III]/ Hβ= 1 for [N II]/ Hα= 0.4, i.e. close to the Kauffmann et al. AGN / HII separation line. These objects are likely to be largely dominated by massive star formation, with non-thermal AGN-like ionization only playing a marginal role, if any, but with weak shocks still being possible. For all objects and all components, the ionization parameter is quite strong. These results are summarized in Column (10) in Table 2.

3.2 Additional Radio Data at 1.4 GHz and WISE Infrared Data

We have searched the FIRST radio survey for counterparts of our candidates at 1.4 GHz. Five sources have been found in the FIRST source catalog, whose flux limit is on average 1 mJy across the surveyed area. However, from a close examination of the FIRST image cutouts, seven more detections were found, all with close positional coincidences (less than $2''$). Two of these remain quite marginal and the derived fluxes may have large uncertainties. All sources are unresolved except for J023832+023349 (alias PKS 0235+023) which is a radio galaxy exhibiting structure in its image. J094430+435421 has a slightly elongated radio image along the north-south direction, but appears to be located in a quite noisy area polluted by ripples that could be due to sidelobe effects from a distant bright source in the same field. The radio data derived from FIRST are listed in Table 3. We have also examined the NVSS survey, but the angular resolution is much better in FIRST ($5''$ instead of $45''$), although the sensitivity to weak extended structures in NVSS may be better. In the NVSS catalog, three sources are present, namely J023832+023349, J091646+283526 and J135646+102609.

The WISE space experiment (Wright et al. 2010, Mainzer et al. 2011) has provided an all-sky map and source catalog in four spectral bands centered at 3.4, 4.6, 12 and 22 microns. The first two bands are usually dominated by starlight, and the two longest by hot interstellar dust. The spatial

Table 3 Additional FIRST Radio Data for Our Double-peaked NEL Sample from LAMOST DR1

Designation (1)	Max. flux density (2)	Integrated flux (3)	S/N (4)	Note (5)	Ref. (6)
J005407.03+073611.9	0.46	0.48	4.0	P	[2]
J023658.06+024217.9	0.36	0.38	3.0	P	[2]
J023832.67+023349.1	23.2	24.94	142	Ext.	[1,3]
J091646.03+283526.7	5.25	5.76	35	P	[1,3]
J094430.79+435421.4	0.61	0.94	5.0	Ext?, (*)	[2]
J113630.61+135848.8	0.42	0.65	3.5	P	[2]
J121342.90+422202.8	1.84	1.58	12	P	[1]
J131434.73+563419.3	0.74	0.99	5.2	P	[2]
J135207.73+052555.8	0.64	1.26	4.5	P	[2]
J135646.10+102609.0	56.5	59.58	362	P	[1,3]
J140225.68+465817.4	0.64	0.52	4.5	P	[2]
J140231.28+184807.8	0.90	1.04	6.2	P	[1]

Notes: Column (1) LAMOST DR1 designation hhmmss.ss+ddmmss.s (J2000.0); Col. (2) Maximum flux density on source, in mJy beam^{-1}; Col. (3) integrated flux in mJy from FIRST catalog; Col. (4) local S/N on source; Col. (5) P: point-source, Ext: resolved extended source; Col. (6) reference: [1] FIRST source catalog, [2] present work, [3] also in NVSS, (*) indicates possible sidelobe contamination on FIRST map.

Table 4 Additional WISE Infrared Data for Our Double-peaked NEL Sample from LAMOST DR1

Designation (1)	3.4 μm flux (2)	4.6 μm flux (3)	12 μm flux (4)	22 μm flux (5)
J005407.03+073611.9	0.79 ± 0.02	0.60 ± 0.02	3.22 ± 0.18	8.00 ± 1.21
J023658.06+024217.9	2.20 ± 0.07	1.50 ± 0.06	7.55 ± 0.35	9.70 ± 1.80
J023832.67+023349.1	4.00 ± 0.09	5.49 ± 0.12	11.84 ± 0.25	34.15 ± 1.40
J083425.28+283451.3	0.80 ± 0.02	0.57 ± 0.02	2.45 ± 0.16	undetected
J091646.03+283526.7	5.17 ± 0.11	7.75 ± 0.15	23.06 ± 0.41	68.62 ± 2.37
J094430.79+435421.4	0.97 ± 0.02	1.35 ± 0.03	2.22 ± 0.15	6.85 ± 1.16
J100708.01+242039.0	0.69 ± 0.02	1.00 ± 0.03	1.88 ± 0.15	4.25 ± 1.37
J104718.31+254348.3	0.54 ± 0.02	0.88 ± 0.02	1.63 ± 0.18	6.52 ± 1.18
J113630.61+135848.8	1.21 ± 0.03	0.94 ± 0.03	3.76 ± 0.20	5.92 ± 1.51
J121342.90+422202.8	2.75 ± 0.06	1.97 ± 0.05	6.50 ± 0.25	19.65 ± 1.33
J123314.49+262624.9	0.40 ± 0.01	0.56 ± 0.02	1.25 ± 0.14	undetected
J131434.73+563419.3	0.71 ± 0.02	0.66 ± 0.02	5.39 ± 0.16	9.68 ± 0.93
J133730.29−002525.4	0.68 ± 0.02	0.58 ± 0.02	3.37 ± 0.16	5.91 ± 0.86
J133737.82+555816.7	0.22 ± 0.01	0.28 ± 0.01	0.93 ± 0.12	undetected
J135207.73+052555.8	5.25 ± 0.15	2.53 ± 0.10	6.63 ± 0.30	9.50 ± 1.80
J135646.10+102609.0	2.23 ± 0.05	4.47 ± 0.09	29.19 ± 0.46	178.83 ± 4.37
J140225.68+465817.4	0.86 ± 0.02	0.66 ± 0.02	5.18 ± 0.16	8.42 ± 0.77
J140231.28+184807.8	0.36 ± 0.01	0.48 ± 0.02	2.45 ± 0.12	9.16 ± 0.82
J150501.56+371311.7	3.93 ± 0.09	4.67 ± 0.09	11.42 ± 0.25	27.30 ± 1.04
J232703.17+004256.7	1.06 ± 0.03	0.68 ± 0.02	1.77 ± 0.17	undetected

Notes: Column (1) LAMOST DR1 designation hhmmss.ss+ddmmss.s (J2000.0); Cols. (2)–(5) WISE flux of source, in mJy, computed from magnitudes in the AllWISE Catalog, for passbands 3.4, 4.6, 12 and 22 μm. For three sources resolved in subcomponents, the fluxes of components were added. The 22 μm fluxes have been corrected following Jarrett et al. (2013). A source is considered to be undetected if its S/N is lower than 3.

resolution is excellent ($6''$ in the three shortest bands, $12''$ in the fourth one) and the sensitivity is very high. We have searched the AllWISE catalog for counterparts to our objects.

The results are given in Table 4, where WISE magnitudes have been converted to fluxes in millijanskys using the recommendations of Jarrett et al. (2013). All sources are detected in the first three bands. In the 22 μm band four objects have an S/N below the formal detection threshold. Three sources (J023658.06+024217.9, J121342.90+422202.8, J135207.73+052555.8) are fitted with two Gaussian point-source components by the catalog construction pipeline, implying there is resolved structure.

3.3 Notes on Individual Objects

We report here some remarks from the SDSS images and references on previous work related to two objects.

J005407+073611: no morphological information available (technical problems in the SDSS image).

J023658+024217: an Sb spiral with a bright nucleus. In a close group with several galaxies whose appearances suggest a similar redshift. The absorption lines could also be double, but this needs confirmation with higher S/N. The SDSS redshift corresponds to the velocity of the blue NEL component.

J023832+023349 (PKS 0235+023): a broad line Seyfert 1 galaxy, probably SBa type, whose $\mathrm{H}\alpha$ broad line exhibits double peaks or twin shoulders. This was fitted quite well, using observations from 1991, with a model attributing the broad emission to a circular, relativistic, Keplerian disk

(Eracleous & Halpern 1994, 2003). However, Gezari et al. (2007) presented long-term monitoring of the double-peaked broad Hα emission lines and found a dramatic change in profile shape after 1991 leading one to consider the simple circular disk model is insufficient for interpretation of the spectra taken after 1991. The present LAMOST spectrum not only shows a double peak on the Hα broad component, but also double peaks on all *narrow* lines including [OII], [NeIII] and [NeV] as well as the Balmer series. The broad component seems highly obscured by internal extinction, since it is almost invisible in Hβ. It is clear that this object deserves detailed follow-up observations.

J083425+283451: an SBb spiral with a low-excitation emission spectrum.

J091646+283526: a quite amorphous galaxy with a perturbed morphology. The bright nucleus is close ($2'' - 3''$) to a second, much redder one. A moderately broad component is present in the Balmer emission lines. The excitation is very strong with bright HeII and [NeV] lines (Seyfert 1.5). This object is a very good merger candidate. The NVSS map shows an extended source with two components, one being approximately coincident with the optical object. Fu et al. (2011a) place J091646+283526 in the category of unresolved narrow-line regions from integral field spectroscopy. They argue that most of these spatially unresolved double-peaked NEL AGNs are aligned or young outflows.

J094430+435421: a QSO whose NELs are well separated. The Hβ line is coincident with the telluric A band of oxygen making spectrophotometry uncertain.

J100708+242039 and J104718+254348: QSOs on which little information is available. The latter is an X-ray source.

J113630+135848: a $\sim$ amorphous galaxy with a possible pair of opposite, low surface brightness, blue diffuse extensions.

J121342+422202: a galaxy with an extended asymmetric envelope. The Hα range is lacking on the SDSS spectrum. A small diffuse object is very close. The galaxy is a member of a group of more than ten objects of similar redshift, among which there is a Seyfert 1 at $4.1'$ north, representing a possible merger or post-merger.

J123314+262624: a QSO, no information.

J131434+563419: peculiar asymmetrically-shaped, possibly barred, galaxy with a blue extension that could be a tidal tail. A possible merger candidate. In a loose group with other galaxies showing similar redshift.

J133730–002525: a spiral galaxy (Sbc/Sc) seen close to face-on, with many faint objects close-by (but no redshift information on them, except one at $5'$ northeast).

J133737+555816: a QSO, no information.

J135207+052555: a typical luminous Seyfert 2 galaxy that is early-type (SO or SO/a). The nucleus appears unique at the spatial resolution of the SDSS image. The double-lined character of the NEL is especially obvious on the [S II] lines which appear as a triple peak. This object is a member of the Abell 1809 galaxy cluster.

J135646+102609: aroused great interest in recent literature. Liu et al. (2010b) included this object in a sample of type 2 AGNs with double-peaked NEL. Its morphology is clearly disturbed, suggesting an ongoing merger. In a loose cluster with several other less luminous objects. The red NEL component has the same redshift as the absorption lines of the stellar population. The presence of two merging galactic nuclei has been demonstrated from optical (Greene et al. 2009, 2011; Fu et al. 2011a) and near-infrared (Shen et al. 2011) observations. Greene et al. (2012) have published two long-slit Magellan LDSS-3 spectra and additional spectral band data. They consider that this object is a pair of interacting galaxies that hosts a luminous obscured quasar in its northern nucleus. Note that the optical spectrum from LAMOST or SDSS is that of a typical unobscured Seyfert 2 galaxy, with all lines being narrow.

J140225+465817: a galaxy with perturbed morphology, with an extension (or projected close companion) along the northeast and irregular fuzzy extension along the south. A possible merger candidate. Isolated.

J140231+184807: a galaxy with a small apparent diameter that seems isolated.

J150501+371311: a galaxy with a bright nucleus and a pear-shaped disk. A diffuse blue object, is at $25''$ east, without redshift information.

J232703+004256: a $\sim$ amorphous galaxy (maybe Sa), forming an interactive pair with a companion at $25''$ northeast, with similar size and brightness. A diffuse matter bridge is seen between both objects, and a tidal tail appears towards the southwest. A single nucleus appears at the resolution of SDSS.

3.4 Possible Origins for Double NEL Structures

3.4.1 Black hole binaries

One initial aim of this investigation was the quest for QSO and AGN candidates hosting binary black holes from the identification of double-peaked NEL in optical spectra, as described by Wang et al. (2009), Liu et al. (2010b; 2011) and Smith et al. (2010). Galaxy nuclei candidates appeared in our sample with consistent "blue" and "red" velocity systems in all the emission lines (i.e., Hβ, [O III] $\lambda\lambda$ 4959, 5007, [N II]$\lambda\lambda$ 6548, 6584, Hα and [S II]$\lambda\lambda$ 6717, 6731) of which five examples are shown in Figure 2. Among the 15 galaxies identified, six exhibit pairs of NEL components that may be unambiguously classified as AGNs. The question remains whether these double NEL systems correspond to double supermassive black hole engines. In addition, five QSOs are identified, among which one (J094430+435421) exhibits a clear case of double NEL components but only has faint radio emission.

In general, statistical analysis of double-peaked [O III] AGN samples by Shen et al. (2011) and Fu et al. (2012) tend to support the conclusion that a large fraction of the double-peak systems are driven by NLR dynamics instead of the existence of black hole binaries. Ge et al. (2012) only found 54 dual-core galaxies with projected separations closer than $3''$ among a sample of 15 600 objects with double-peaked or asymmetric NELs, but the angular resolution of SDSS images is not sufficient to disentangle the very close components.

We also stress that previous studies of double-peaked NELs have focused on very obvious, well separated double lines in the line profiles, which have been observed for a long time but remain largely unexplained. In the present limited sample, with the available low or moderate spatial and spectral resolutions (optical spectra, SDSS images and FIRST radio maps), we do not find evidence for binary nuclei as exhibited by the already well-known binary BH candidates (Ge et al. 2012), except in J091646+2835, which has two central condensations and has a double AGN-like spectrum that shows an NEL component. (Note that the well-studied case J135646+102609 does not show up as clearly as a binary nucleus merger on the SDSS images.) This study hence must be completed with additional higher resolution images that are taken under good seeing conditions, and other multi-band data from follow-up observations.

3.4.2 Interaction between jet and NLR

In radio-loud AGNs, a double narrow line structure may readily arise from the radio-jet interaction with the NLR clouds. This mainly operates by ram pressure acceleration of the ionized gas clouds producing the NLR, that can produce complicated NLR kinematics, and especially double lines, due to projection on the line of sight of the cone structure in the matter participating in the interaction. If the jet (whose direction points approximately towards the observer) drags and accelerates matter associated with the NLR matter with it, a Doppler blueshifted (with respect to the systemic redshift) ionized gas component may naturally appear in the spectrum. Note that Smith et al. (2010) exclude radio-loud AGNs from their candidate binary black hole because they think that these objects are more or less dominated by the jet / NLR interaction. The literature on these phenomena is quite

extensive, and there have been extremely detailed studies on some nearby cases; most of them are Seyfert 2 galaxies (see e.g. Whittle et al. 2005, Rosario et al. 2008 with many references therein), for which high spatial resolution optical and radio mapping is possible.

In our double-peaked NEL sample, the objects detected at 1.4 GHz that have the largest radio flux (corresponding more or less to the largest radio luminosity) have their NEL components arising from type AGN + AGN with FWHM values larger than average (typically larger than 350 $\mathrm{km\ s^{-1}}$). It should be useful to explore if this trend still holds in larger samples.

3.4.3 Interaction with companion galaxies and merger candidates

Galaxy collisions and subsequent merging are natural sources of double emission line phenomena, depending on the spatial integration of the spectrograph's entrance aperture, on the angle of projection of the interacting system with respect to the line of sight and on the observed collision phase. Since interactions between gas-rich systems are likely to enhance star formation, ionized gas could be observed in the two components of a strongly interacting system with velocity separations up to a few hundred $\mathrm{km\ s^{-1}}$. These interactions are accompanied by many morphological perturbations, such as tidal tails, matter bridges, deformation of disks, asymmetric envelope extensions, etc. Also, several authors have proposed that nuclear activity may sometimes be triggered by galaxy interactions.

In the present sample, examination of the SDSS images leads to finding one clear interacting pair (J232703+0042), one merger (J135646+1026), four candidates mergers or possible candidate mergers (J091646+2835, J121342+4222, J131434+5634, J140225+4658), two more objects that have perturbed morphology (J113630+1358, J150501+3713) and J135207+0525 belonging to a populated cluster in which encounters should have higher probability than in the field. Thus, 2/3 of our $galaxy$ sample are objects for which interaction is a plausible origin for the NEL double structure. Verification of this hypothesis, its extension to other double-peaked NEL galaxy samples and better modeling cannot be done without follow-up observations, including deep imagery.

Regarding the QSO, for which morphology information is not available, several previous authors (Hutchings et al. 1982; Malkan et al. 1984; Green & Yee 1984) have noted that low-redshift quasars very often have faint companion galaxies with small projected angular separations. A scenario involving a collision between a giant AGN host galaxy and a gas-rich star-forming dwarf may lead to a double structure in the NEL of the AGN; in the process of interaction, the companion is disrupted by the tidal field of the giant galaxy. Clumps of its interstellar matter may approach the AGN sufficiently close such that these clumps may experience violent differential accelerations able to increase their velocity dispersion up to significantly higher values than the usual average value of the quiet disk. If interaction with a neighbor were the origin of the double structure in an AGN NEL, observations could disentangle the ionized gas of the companion, expected to have line ratios consistent with photoionization from normal massive stars, so that the NLR component of the AGN in which the ionization is basically due to spectra from a non-thermal source. The present sample does not enable this conclusion for the QSO, because $\mathrm{H}\alpha$ is not observed.

4 SUMMARY

We present a search for double-peaked NEL galaxies and AGNs in the LAMOST survey spectroscopic database. Applying our method to LAMOST DR1, we find 20 candidates, among which ten are original discoveries. Spectra from SDSS, available for 17 objects, confirm their double-peaked narrow-line profiles. We report new weak radio continuum fluxes and give the position of each NEL component in the BPT diagnostic diagram for 15 objects. We briefly discuss some possibilities about the origin of the double components in emission lines, and emphasize that our galaxy subsample appears dominated by objects likely to participate in gravitational interaction with neighbors or ongoing merging processes. The double-peaked sample can be used to study the dynamical processes

of merging galaxies, jet-cloud interactions, and gas kinematics in the narrow-line regions. With the ongoing progress of the LAMOST survey, we shall be able to enlarge the sample and perform statistical analysis on the population of double-peaked NEL galaxies and AGNs. For the current sample, additional high resolution optical and multi-band follow-up observations are needed to understand the origins of the double components in emission lines.

Acknowledgements This study is supported by the National Natural Science Foundation of China (Grant Nos. 10973021, 11233004 and 61202315) and the National Basic Research Program of China (973 Program, 2014CB845700). The Guo Shou Jing Telescope (the Large Sky Area Multi-Object Fiber Spectroscopic Telescope, LAMOST) is a National Major Scientific Project built by the Chinese Academy of Sciences. Funding for the project has been provided by the National Development and Reform Commission. LAMOST is operated and managed by National Astronomical Observatories, Chinese Academy of Sciences. The LAMOST Data Release 1 website is *http://data.lamost.org/dr1/*. This publication makes use of data products from the Wide-field Infrared Survey Explorer, which is a joint project of the University of California, Los Angeles, and the Jet Propulsion Laboratory/California Institute of Technology, funded by the National Aeronautics and Space Administration. Funding for SDSS-III has been provided by the Alfred P. Sloan Foundation, the Participating Institutions, the National Science Foundation, and the U.S. Department of Energy Office of Science. The SDSS-III website is *http://www.sdss3.org/*. The FIRST website is *http://sundog.stsci.edu/*. The NVSS website is *http://www.cv.nrao.edu/nvss/*. G. C. expresses his deepest thanks to the Chinese Academy of Sciences for the award of a Visiting Professorship for Senior International Scientists under Grant No. 2010T2J19.

References

Alongi, M., Bertelli, G., Bressan, A., et al. 1993, A&AS, 97, 851
Baldwin, J. A., Phillips, M. M., & Terlevich, R. 1981, PASP, 93, 5
Barrows, R. S., Stern, D., Madsen, K., et al. 2012, ApJ, 744, 7
Blecha, L., Loeb, A., & Narayan, R. 2013, MNRAS, 429, 2594
Bruzual, G., & Charlot, S. 2003, MNRAS, 344, 1000
Cardelli, J. A., Clayton, G. C., & Mathis, J. S. 1989, ApJ, 345, 245
Chabrier, G. 2003, PASP, 115, 763
Chen, X. Y., Liang, Y. C., Hammer, F., Zhao, Y. H., & Zhong, G. H. 2009, A&A, 495, 457
Cid Fernandes, R., Mateus, A., Sodré, L., Stasińska, G., & Gomes, J. M. 2005, MNRAS, 358, 363
Civano, F., Elvis, M., Lanzuisi, G., et al. 2012, ApJ, 752, 49
Comerford, J. M., Gerke, B. F., Newman, J. A., et al. 2009a, ApJ, 698, 956
Comerford, J. M., Gerke, B. F., Stern, D., et al. 2012, ApJ, 753, 42
Comerford, J. M., Griffith, R. L., Gerke, B. F., et al. 2009b, ApJ, 702, L82
Comerford, J. M., Pooley, D., Gerke, B. F., & Madejski, G. M. 2011, ApJ, 737, L19
Cui, X.-Q., Zhao, Y.-H., Chu, Y.-Q., et al. 2012, RAA (Research in Astronomy and Astrophysics), 12, 1197
Eracleous, M., & Halpern, J. P. 1994, ApJS, 90, 1
Eracleous, M., & Halpern, J. P. 2003, ApJ, 599, 886
Fischer, T. C., Crenshaw, D. M., Kraemer, S. B., et al. 2011, ApJ, 727, 71
Fu, H., & Stockton, A. 2009, ApJ, 696, 1693
Fu, H., Myers, A. D., Djorgovski, S. G., & Yan, L. 2011a, ApJ, 733, 103
Fu, H., Zhang, Z.-Y., Assef, R. J., et al. 2011b, ApJ, 740, L44
Fu, H., Yan, L., Myers, A. D., et al. 2012, ApJ, 745, 67
Ge, J.-Q., Hu, C., Wang, J.-M., Bai, J.-M., & Zhang, S. 2012, ApJS, 201, 31
Gelderman, R., & Whittle, M. 1994, ApJS, 91, 491
Gerke, B. F., Newman, J. A., Lotz, J., et al. 2007, ApJ, 660, L23

Gezari, S., Halpern, J. P., & Eracleous, M. 2007, ApJS, 169, 167
Green, R. F., & Yee, H. K. C. 1984, ApJS, 54, 495
Greene, J. E., Zakamska, N. L., Liu, X., Barth, A. J., & Ho, L. C. 2009, ApJ, 702, 441
Greene, J. E., Zakamska, N. L., Ho, L. C., & Barth, A. J. 2011, ApJ, 732, 9
Greene, J. E., Zakamska, N. L., & Smith, P. S. 2012, ApJ, 746, 86
Hutchings, J. B., Campbell, B., Gower, A. C., Crampton, D., & Morris, S. C. 1982, ApJ, 262, 48
Jarrett, T. H., Masci, F., Tsai, C. W., et al. 2013, AJ, 145, 6
Kauffmann, G., Heckman, T. M., Tremonti, C., et al. 2003, MNRAS, 346, 1055
Kewley, L. J., Dopita, M. A., Sutherland, R. S., Heisler, C. A., & Trevena, J. 2001, ApJ, 556, 121
Komossa, S., Burwitz, V., Hasinger, G., et al. 2003, ApJ, 582, L15
Liu, X., Shen, Y., Strauss, M. A., & Greene, J. E. 2010a, ApJ, 708, 427
Liu, X., Greene, J. E., Shen, Y., & Strauss, M. A. 2010b, ApJ, 715, L30
Liu, X., Shen, Y., Strauss, M. A., & Hao, L. 2011, ApJ, 737, 101
Liu, X., Civano, F., Shen, Y., et al. 2013, ApJ, 762, 110
Luo, A.-L., Zhang, Y.-X., & Zhao, Y.-H. 2004, in Society of Photo-Optical Instrumentation Engineers (SPIE) Conference Series, 5496, Advanced Software, Control, and Communication Systems for Astronomy, eds. H. Lewis, & G. Raffi, 756
Luo, A.-L., Zhang, H.-T., Zhao, Y.-H., et al. 2012, RAA (Research in Astronomy and Astrophysics), 12, 1243
Mainzer, A., Bauer, J., Grav, T., et al. 2011, ApJ, 731, 53
Malkan, M. A., Margon, B., & Chanan, G. A. 1984, ApJ, 280, 66
McGurk, R. C., Max, C. E., Rosario, D. J., et al. 2011, ApJ, 738, L2
Rosario, D. J., McGurk, R. C., Max, C. E., et al. 2011, ApJ, 739, 44
Rosario, D. J., Shields, G. A., Taylor, G. B., Salviander, S., & Smith, K. L. 2010, ApJ, 716, 131
Rosario, D. J., Whittle, M., Nelson, C. H., & Wilson, A. S. 2008, Mem. Soc. Astron. Italiana, 79, 1217
Schlegel, D. J., Finkbeiner, D. P., & Davis, M. 1998, ApJ, 500, 525
Shen, Y., Liu, X., Greene, J. E., & Strauss, M. A. 2011, ApJ, 735, 48
Smith, K. L., Shields, G. A., Bonning, E. W., et al. 2010, ApJ, 716, 866
Smith, K. L., Shields, G. A., Salviander, S., Stevens, A. C., & Rosario, D. J. 2012, ApJ, 752, 63
Stockton, A., Canalizo, G., Fu, H., & Keel, W. 2007, ApJ, 659, 195
Wang, J.-M., Chen, Y.-M., Hu, C., et al. 2009, ApJ, 705, L76
Wang, X.-W., & Zhou, H.-Y. 2012, ApJ, 757, 124
Whittle, M., Rosario, D. J., Silverman, J. D., Nelson, C. H., & Wilson, A. S. 2005, AJ, 129, 104
Wright, E. L., Eisenhardt, P. R. M., Mainzer, A. K., et al. 2010, AJ, 140, 1868
Xu, D., & Komossa, S. 2009, ApJ, 705, L20
Yao, S., Liu, C., Zhang, H.-T., et al. 2012, RAA (Research in Astronomy and Astrophysics), 12, 772
Zhao, G., Zhao, Y.-H., Chu, Y.-Q., Jing, Y.-P., & Deng, L.-C. 2012, RAA (Research in Astronomy and Astrophysics), 12, 723
Zhou, H., Wang, T., Zhang, X., Dong, X., & Li, C. 2004, ApJ, 604, L33